



# Deformation and interlaminar crack propagation sensing in carbon fiber composites using electrical resistance measurement

Hyung Doh Roh, Soo-Young Lee, Eonyeon Jo, Hyegyu Kim, Wooseok Ji\*, Young-Bin Park\*

Department of Mechanical Engineering, Ulsan National Institute of Science and Technology, UNIST-gil 50, Ulsu-gun, Ulsan 44919, Republic of Korea

## ARTICLE INFO

### Keywords:

Non-destructive evaluation  
Structural health monitoring  
Mode I testing  
Delamination growth  
Finite element method

## ABSTRACT

In this study, we propose analytical and experimental methods to predict and detect deformation and interlaminar crack propagation in carbon fiber-reinforced plastics (CFRPs) based on electrical resistance measurement. The electromechanical behavior of CFRP was investigated from the elastic region to crack propagation. The CFRPs were subjected to tensile, three-point bending, and Mode I dual cantilever beam loads, and the signature electromechanical response was correlated to subsequent deformations and crack propagation. The self-sensing investigation was extended to different fiber combinations and electrode placement schemes to obtain customized sensitivity. The experimental results were verified through finite element analysis. In parallel, equivalent electrical circuit modelling was conducted to obtain the “resistor components” that exist in a CFRP and predict the electromechanical behavior under various mechanical loads.

## 1. Introduction

In recent years, structural health monitoring (SHM) methods with fiber-reinforced plastic (FRP) have gained attention from engineers with the increasing number of FRP structures in various fields [1–4]. Both array-type [5–14] and hybrid type [15–19] sensing systems are widely used for large-scale composite structures. They require not only numerous data acquisition channels but also various sensing devices attached to the structures.

Among the various types of FRPs, carbon fiber-reinforced plastic (CFRP) has seen increasing demand, because it has superior mechanical properties to those of glass fiber-reinforced plastic (GFRP). CFRP possesses self-sensing capabilities, because it has electrical conductivity, and its electrical resistance changes upon application of a mechanical strain [20–23].

Todoroki et al. [24–26] investigated the electrical resistance changes in unidirectional CFRPs under various loading and damage conditions. Swait et al. [27] and Schueler et al. [28,29] developed a similar mechanism with an array-form to monitor the structure section by section. In addition, the multi-axial electromechanical behavior of CFRP was analyzed in the form of a tensor similar to the laminate plate theory, considering the surface piezoresistivity [30,31].

However, woven-CFRP self-sensing with respect to delamination has been limited. *In situ* self-sensing of crack propagating has been absent, and hence, the analysis of crack length in condition-based monitoring

has not been possible. Moreover, investigations of carbon-glass hybrid fiber reinforced plastic (HFRP), which is a compromising material between mechanical performance and cost, have also been lacking. Therefore, the self-sensing capabilities of CFRPs and HFRPs were investigated under tensile, three-point bending, and mode-I dual cantilever beam (DCB) tests. Furthermore, finite element analysis (FEA) was utilized to obtain the mechanical stress along the specimen length, and to analyze the effective range of the electrical resistance measurement method. The final objective of the study was to realize self-sensing of real-time crack-propagation and SHM of carbon fiber composites using only the electrical resistance measurement without any additional treatments or sensing devices.

## 2. Experimental

### 2.1. Materials

DBLT 850-E glass fiber (Cymax, Taiwan) and 3 K plain-woven carbon fiber (Mitsubishi, Japan) were purchased from Jet Korea Corp. (Changwon, Korea). DBLT 850-E glass fiber is a quadra-axial glass fiber with a stacking sequence of 0/+45/−45/90°, density of 850 g/m<sup>2</sup>, and a thickness of ~0.6 mm. The density of 3 K plain-woven carbon fiber with a thickness of ~0.2 mm was 305 g/m<sup>2</sup>. Carbon-glass hybrid fiber, whose warp or weft is 3 k carbon fiber tow, and the other is 3 k glass fiber tow, was purchased from JMC corp. The polymer matrix used was

\* Corresponding authors.

E-mail address: [ypark@unist.ac.kr](mailto:ypark@unist.ac.kr) (Y.-B. Park).

<https://doi.org/10.1016/j.compstruct.2019.02.100>

Received 24 November 2018; Received in revised form 10 February 2019; Accepted 25 February 2019

Available online 26 February 2019

0263-8223/© 2019 Elsevier Ltd. All rights reserved.

vinylester which consists of 45% styrene and 55% epoxy acrylate (RF-1001MV, Epovia), and its corresponding catalyst (cobalt-naphthenate, Jet Korea) and curing agent (methyl ethyl ketone peroxide, Arkema) were mixed with 0.5 and 1.0 wt.% of the polymer, respectively. The polymer, catalyst, and curing agent were obtained from Jet Korea Corp. (Changwon, Korea).

## 2.2. Specimen manufacturing process

Composite specimens were manufactured using vacuum-assisted resin transfer molding (VARTM). Before resin infusion, electrodes were embedded in the fabric using silver paste to obtain stable electrical contact.

Flexural bending specimens were composed of 12 carbon fiber plies, and electrodes were placed on the second and tenth carbon fiber plies, 80 mm apart, as shown in Fig. 1(a). The bending specimen was 200 mm in length and 40 mm in width.

DCB specimens consisted of 24 plies of 3k plain-woven carbon fiber or carbon-glass hybrid fiber, and a major portion of the experimental procedure followed ASTM D5528-13, which is for the mode-I testing of unidirectional FRPs. Regarding HFRP orientation, the glass fiber was placed length-wise while the carbon fiber was placed width-wise. The DCB specimen was 200 mm in length, 40 mm in width, and 2.5 mm in thickness. A 60 mm-long polytetrafluoroethylene (PTFE) film was inserted in the mid-plane (between the 12th and 13th plies) of the specimen before infusion to create the initial crack, as shown in Fig. 1(b). A piano hinge made of two stainless steels (SUS304) with a length of 20 mm was attached at both the top and the bottom surface for the mode-I test grid. Epoxy adhesive (Hysol E-120P, Loctite) was used after polishing the surfaces with 120 and 400 grit-sand papers in sequence.

Two types of electrode placements were employed for the DCB specimens to compare the electromechanical sensing performances. Four electrodes were placed lengthwise on the carbon fiber along the center line, each 30 mm apart in one plane. The first type involved embedding this set on the 2nd and 22nd carbon fiber plies, as shown in Fig. 1(b). The other involved embedding the electrode sets on the 10th and 14th carbon fiber plies, which have a shorter electrode distance (Fig. 1(c)). The through-thickness distance between the electrodes determines whether the specimen has a longer or shorter inter-electrode distance; for example, the specimen in Fig. 1(b) has a longer inter-electrode distance, whereas the specimen in Fig. 1(c) has a shorter inter-electrode distance.

## 2.3. Characterization

The bending test of 10-ply-FRPs was conducted using a hydraulic testing machine (STC corp., Korea) with a compressive loading rate of 6 mm/min until failure, as shown in Fig. 2(a).

The flexural test of 12-ply-CFRPs was conducted using a universal testing machine (Instron 5982, USA) with a three-point bending jig. The support span was 120 mm, and the loading rate was 2.5 mm/min initiated with 2 N preload. The support span was determined by the span to thickness ratio suggested in ASTM D790 [32]. The ratio used in this section was 50:1.

The mode-I delamination test was performed using a hydraulic testing machine (STC Corp., Korea) with a tensile extension rate of 5 mm/min. The machine gripped the stainless piano hinges on the specimen. A digital camera captured an image of the testing procedure every second to determine the crack propagation length, as shown in Fig. 2(b). Image analysis (Fig. 2(c)) was conducted to calculate the crack length based on the number of pixels in the captured image through the in-house algorithm written in MATLAB. The pixels in the propagating crack were distinguished based on the greyscale contrast; hence, the specimen was painted in white and the background panel was in black to maximize the contrast difference. The algorithm binarized the obtained images with respect to the threshold

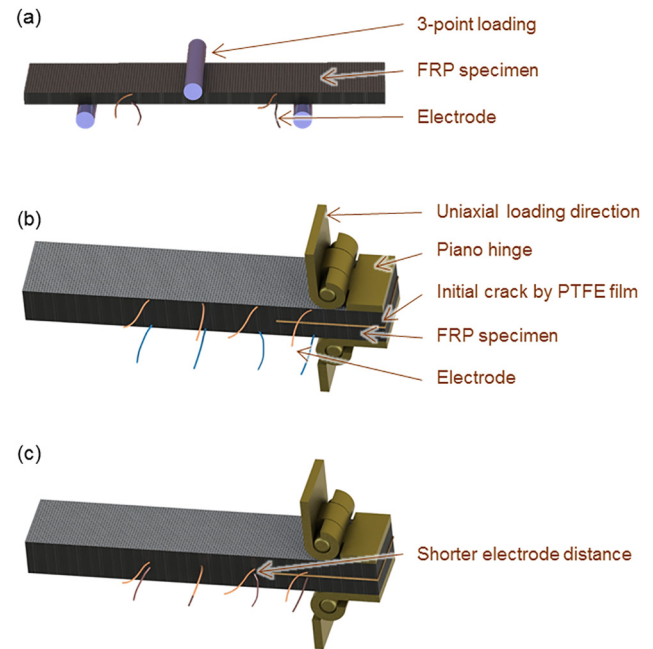


Fig. 1. (a) CFRP specimen for three-point bending test, (b) CFRP DCB specimen for mode-I test, and (c) that of shorter electrode distance.

correspondent with the greyscale intensity of a pixel in the crack region. A 2D median filter, replacing the greyscale value of each pixel with the median value of 8 surrounding elements, was applied to reduce several outliers in each image, such as black pixels inside the beam region due to painting quality. From the user-defined two initial search windows, indicated as red<sup>1</sup> dotted boxes in Fig. 3, the algorithm searched for the coordinate of the black pixel in the crack-tip and the coordinate of the white pixel in the beam-tip. Then, the algorithm automatically defined the tip-centered search windows for the next image. Following the aforementioned working principle, the coordinates of the propagating crack-tip and beam-tip in every image were obtained in each local coordinate system (LCS) of search windows. The crack length can be calculated by converting the coordinates of the two tips into the global coordinate system (GCS). Finally, the crack length can be calculated as the difference between the initial beam length and obtained remaining beam length.

The aforementioned mechanical investigations were accompanied with electrical resistance measurement using a digital multimeter (Keithley 2002, USA) and a switching module (Keithley 7001, USA), simultaneously. The switching module enabled sequential measurement of the designated electrode pairs automatically at a maximum sampling rate of ~44 points per second. For each experimental set, measurements were made at least three times. Although the two-probe measurement may be affected by the contact resistance, the percent change in electrical resistance obtained as such can effectively be used for crack propagation monitoring purposes [21–23,26,27,29].

## 2.4. FEA simulations

The commercially available FEA software, ABAQUS, was utilized to investigate the mechanical resultants of the DCB tests, and hence to rationalize the electromechanical behavior. To investigate the mechanical stress during the DCB tests, a CFRP in the simulation consisted of 24 homogeneous layers with a thickness of 0.2 mm and cohesive layers with a thickness of 0.001 mm between each lamina. In addition,

<sup>1</sup> For interpretation of color in Figs. 3 and 5, the reader is referred to the web version of this article.

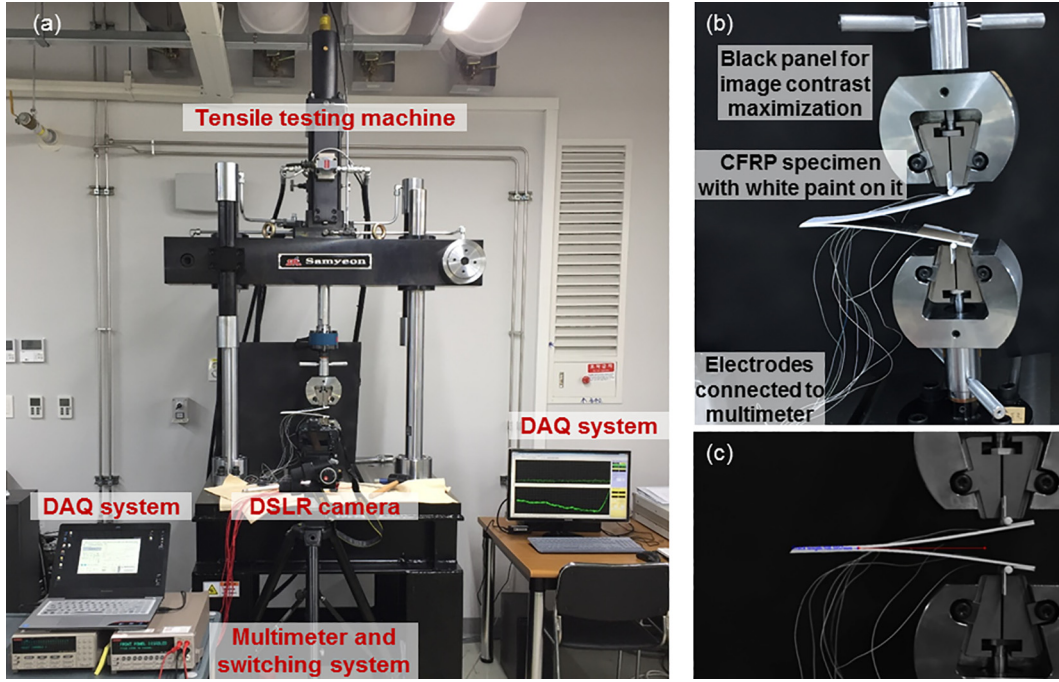


Fig. 2. (a) Experimental setup of DCB test, (b) Capturing photos during the DCB test, (c) Image processing to calculate the crack length.

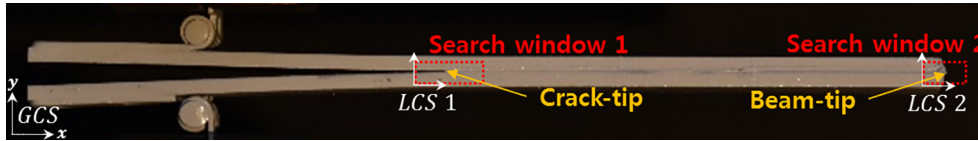


Fig. 3. Image analysis algorithm for crack length acquisition by setting the local coordinate system (LCS).

aluminum hinges were attached at the edges of the CFRP, and the tensile extension was applied to the hinges to realize the experimental setup. Independent quad-structured meshes were set; 488,216 linear quadrilateral CPS4 for the hinges and the laminae, and 5800 linear quadrilateral COH2D4 for the cohesive. Regarding physical properties, the Hashin criteria, Eq. (1) for tensile and Eq. (2) for compressive, was used for fiber failure. The damage initiation model by the traction separation law (Eq. (3)) and Benzeggah-Kenane law for damage evolution (Eq. (4)) were used to calculate the cohesive zone failure.

$$\left(\frac{\sigma_{11}}{S_{11}}\right)^2 + \left(\frac{\sigma_{11}}{S_{12}}\right)^2 + \left(\frac{\sigma_{11}}{S_{13}}\right)^2 = 1 \quad (1)$$

$$\left(\frac{\sigma_{11}}{X_{1c}}\right)^2 = 1 \quad (2)$$

$$\left(\frac{t_n}{t_n^o}\right)^2 \left(\frac{t_s}{t_s^o}\right)^2 + \left(\frac{t_t}{t_t^o}\right)^2 = 1 \quad (3)$$

$$G_n^c + (G_s^c - G_n^c) \left(\frac{G_s}{G_t}\right)^n = G_t^c \quad (4)$$

The mechanical properties of CFRP are shown in Table 1, those of HFRP in Table 2, and those of the cohesive layer in Table 3.

Electrical analysis was also performed by simulation. The in-plane and through-thickness electrical resistivities for the carbon fiber used were 15 and  $10^6 \Omega\text{-m}$ , respectively, and the electrical resistivity of silver paste, which was applied at the junction between the fiber and the electrodes, was isotropically  $0.001 \Omega\text{-m}$  [33–35]. The element type in the electrical simulation was Q3D8, and the number of elements used for the analysis was 20188.

Table 1  
Mechanical properties of CFRP model.

Mechanical properties of CFRP laminar	
$E_{11} = E_{33}$	61.5 GPa
$E_{22}$	7.7 GPa
$\nu_{12} = \nu_{23}$	0.3
$\nu_{13}$	0.05
$G_{12} = G_{23}$	2.9 GPa
$G_{13}$	3.7 GPa
$X_{1t} = X_{2t}$	840 MPa
$X_{1c} = X_{2c}$	570 MPa
$S_{12}$	72 MPa
Failure coefficient	0

Table 2  
Mechanical properties of HFRP model.

Mechanical properties of HFRP laminar	
$E_{11}$	12 GPa
$E_{22}$	7.7 GPa
$E_{33}$	61.5 GPa
$\nu_{12} = \nu_{23}$	0.25
$\nu_{13}$	0.05
$G_{12} = G_{23}$	2.9 GPa
$G_{13}$	3.7 GPa
$X_{1t}$	550 MPa
$X_{2t}$	840 MPa
$X_{1c}$	313 MPa
$X_{2c}$	570 MPa
$S_{12}$	72 MPa
Failure coefficient	0

**Table 3**  
Mechanical properties of the cohesive elements.

Mechanical properties of the cohesive layer	
$K_n$	1000 MPa
$K_s = K_t$	1000 MPa
$G_n^c$	0.2 N/mm
$G_s^c = G_t^c$	1 N/mm
$t_n$	10 MPa
$t_s = t_t$	20 MPa
$\eta$	1

### 3. Results and discussion

#### 3.1. Failure prognostic behavior of composites

The strain-related electrical resistance change and failure prognostic function of CFRP were obtained from the flexural test. The initial resistances of channels 1–4 were 2.2, 2.2, 2.1, and 2.1  $\Omega$ , respectively. As shown in Fig. 4(b), channel 1 demonstrated a decrease in the electrical resistance until the flexural stress decreased after failure. This is because the adjacent laminae were compacted in the through-thickness direction (inter-ply effect), and tensile strain caused better fiber alignment (intra-ply effect). However, channel 2 demonstrated an increase in electrical resistance because the upper laminae crumpled when the specimen was bent. Channels 3 and 4, which measured the resistance in the thickness direction, demonstrated positive piezoresistivity; the electrical resistance increased following the flexural stress. During bending, the previous electrical conductive network was changed due to the tensile extension at the bottom surface and compressive at the top surface. Interlaminar shear deformations contributed to the change in pre-existing electrical network.

The slopes of channels 2, 3, and 4 decreased at point a and point b marked in Fig. 4(b), which is 63% and 80% of the flexural strength, respectively. Information regarding points a, b, and c in Fig. 4(b) are provided in Table 4. The slope changed due to the internal mechanical states of CFRP specimens; hence, the slope change can be indicative of mechanical failure. Even though FBGs, strain gauges, and C-scan sensors can analyze the structural health in detail, they cannot prognose the structural integrity. However, comparing the electromechanical signals of the tensile and compressive components, it is possible to monitor the mechanical state and residual ultimate life of a CFRP.

#### 3.2. Mode-I delamination test of CFRP

The electrical resistance change ratio of the composites reflected mechanical states during the DCB tests depending on the fiber configurations and electrode location. The fiber configurations determined the electromechanical sensitivity, while the electrode placement determined the sensing range.

**Table 4**  
Prognostic electromechanical behavior of CFRP during three-point bending test.

Point	Time (s)	Stress (MPa)	Ration of the strength (%)
(a)	66	92	63
(b)	84	118	80
(c)	106	147	100

PZT [10] and FBG sensors [12] were used to detect delamination with sensors in an array. To realize self-sensing, some researchers utilized short fiber [20]. Otherwise, Todoroki et al. [26] and Swait et al. [27] embedded electrodes in an array. On the contrary, the crack propagating self-sensing in this research enabled structural health monitoring without introducing any additional sensing device or short fibers. Investigating the correlation between the electrical resistance and the crack length did not necessitate electrode arrays large-scale SHM. While the previous models using the classic laminate plate theory [30,31] covers only the elastic regime, this study extends into the crack-propagating regime.

Among the two types of electrode placements, that with the longer inter-electrode distance in the CFRP DCB specimen demonstrated both prognostic and health monitoring capabilities through electro-mechanical analysis, as demonstrated in Fig. 5. The crack length plot in Fig. 5(b) can detect the location the crack propagated through, while the mechanical load plot in Fig. 5(c) is limited to distinguishing only the first failure.

The number in a circle shown in Fig. 5(a) indicates the distance between the piano hinge and end of the initial crack or virtual electrode set path. This is also indicated in the right ordinate of Fig. 5(b). Orange auxiliary lines in Fig. 5(b) aid in distinguishing the electrical resistance changes with respect to the crack propagation length. Virtual electrode set paths are indicated as colored lines and numbers on the specimen (Fig. 5(a)). Channels 1–4 measured the electrical resistance thickness-wise, and channels 5–7 measured the in-plane resistance. The initial resistances of channels 1–4 were 2.3, 2.1, 2.3, and 2.2  $\Omega$ , respectively, and those of channels 5–7 were 2.3, 2.2, and 2.2  $\Omega$ , respectively. Similar resistance values suggest that there the effects of contact resistance are not significant.

Channel 1 in Fig. 5(b) and (c) showed an increase in the electrical resistance; however, the slope of the resistance was changed near crack initiation, which was similar to the phenomenon shown in Fig. 4(b). After failure (crack initiation), the resistance increased linearly, because the length of the electrical network detour increased after the crack tip.

In Fig. 5(b), ~1% electrical resistance decrease was observed in channels 2, 3, and 4 when the crack approached the vertical imaginary electrical path shown in Fig. 5(a). This resistance decrease indicates that mechanical compression occurred on the effective electrical path. When the crack passed the vertical line, the electrical resistance

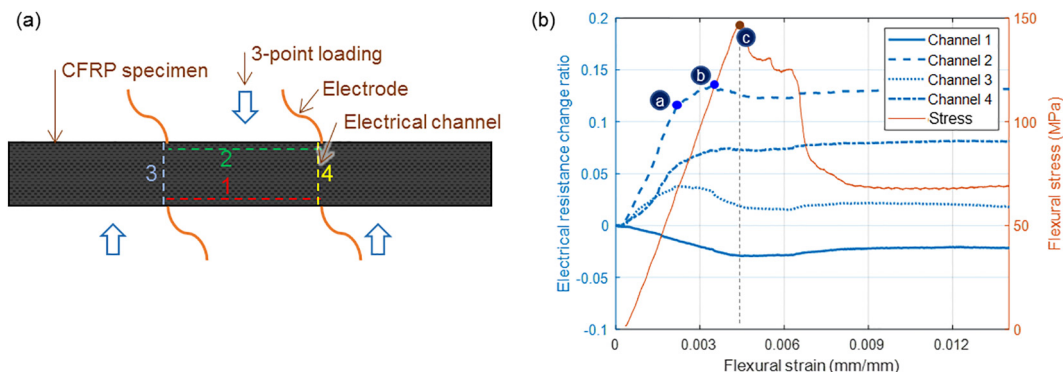


**Fig. 4.** (a) Schematic of three-point bending specimen. (b) Electromechanical behavior of CFRP during three-point bending test.



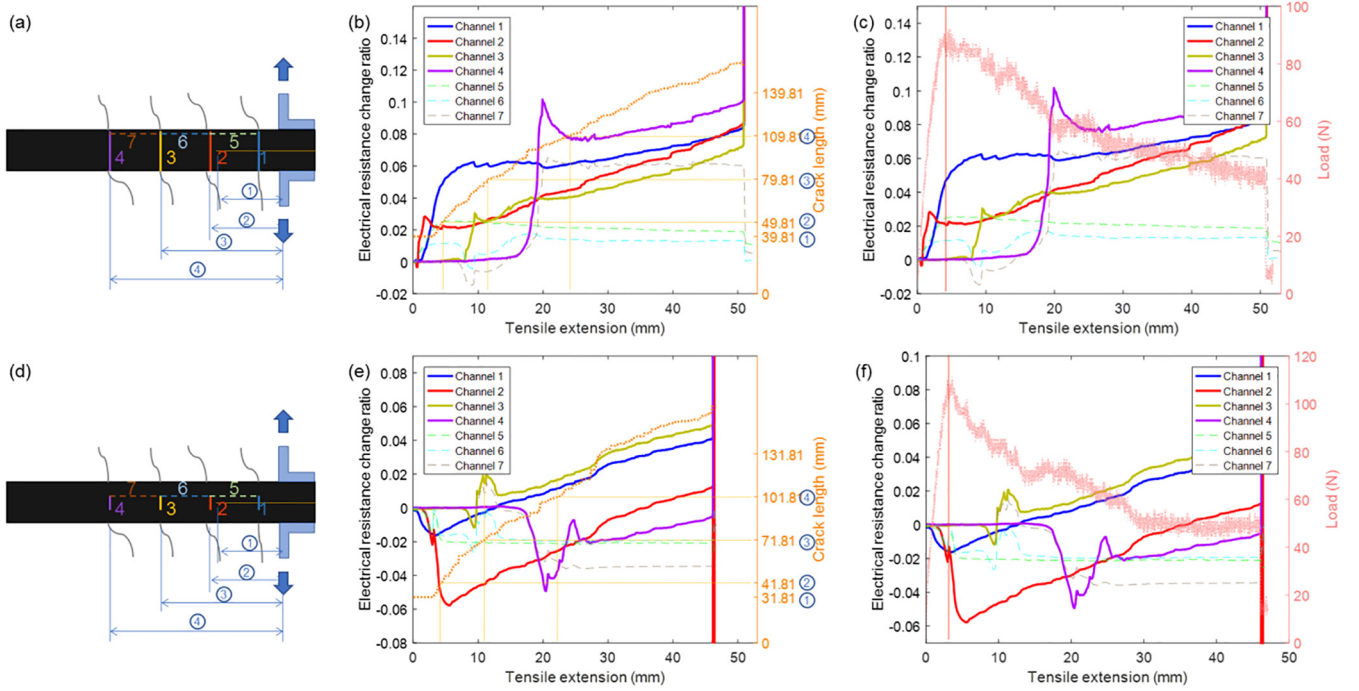


**Fig. 5.** (a) CFRP specimen with longer inter-electrode distance, (b) Electromechanical behavior of the longer inter-electrode distance CFRP compared to crack length, (c) Electromechanical behavior compared to load. (d) CFRP specimen with shorter inter-electrode distance, (e) Electromechanical behavior of the shorter inter-electrode CFRP compared to crack length, (f) Electromechanical behavior compared to load.

increased linearly until the beams were completely separated, because of the electrical detour passing through the electrode, crack tip, and the opposite electrode. The electrical resistance tended to infinity when the beams were completely separated at the tensile extension of 50 mm.

Whereas channels 5–7 demonstrated resistance changes during crack propagation, they rarely demonstrated changes when the crack tip passed by the last electrode set, indicated as number 4 in a circle. When the crack propagated through the last electrode set, bending deformation occurred around channels 5–7, so that the plateau was observed after 22 mm of tensile extension (abscissa of Fig. 5(b)).

The electrical resistance change ratio of the crack passing through the virtual lines shown in Fig. 5(a) can be represented as linear equations. Because crack propagation was also linear with respect to the tensile extension, the crack propagation length can be obtained from the electrical resistance change ratio using the equations below:

$$\text{Channel 1: } y_1 = 0.0013x_1 + 0.0279 \quad (5)$$

$$\text{Crack: } y_2 = 3.1949x_1 - 22 \quad (6)$$

where  $y_1$  is the electrical resistance change ratio of channel 2,  $x_1$  is the tensile extension of the crack mouth, and  $y_2$  is the crack propagation length.  $R^2$  of Eq. (5) was 0.9921, and that of Eq. (6) was 0.9529.

The measured electrical resistance can be converted into the electrical change ratio which is  $y_1$  in Eq. (5). Subsequently, the crack mouth opening length or tensile extension,  $x_1$ , was calculated and substituted into Eq. (6), to calculate the crack propagation length,  $y_2$ .

The shorter inter-electrode specimen, which has electrodes on the 10th and 14th carbon fiber plies, is described in Fig. 5(d). The objective of the shorter inter-electrode placement was to focus on inter-laminar delamination more than in the previous examination.

In this case, electrodes were placed outside the neutral axis, and hence channel 1 in Fig. 5(d) demonstrated a decrease in the electrical resistance at the beginning, as shown in Fig. 5(e). This is because the tension applied at the outer part of the neutral axis resulted in a phenomenon similar to channel 1 in the flexural test (analyzed in Fig. 5(e)).

Channel 2 in Fig. 5(d) also demonstrated a substantial decrease in the electrical resistance (Fig. 5(e)) compared with that of the longer

inter-electrode specimen, even though beam bending was not applied near channel 2. This might be triggered by inter-laminar compressive deformation in the thickness direction, which will be discussed during simulation.

Channels 3 and 4 also demonstrated a decrease in electrical resistance due to compression when the crack tip approached the virtual lines and increase in resistance when the crack propagated through the virtual lines, also indicated as numbers in a circle in Fig. 5(d). Channels 5–7 demonstrated similar results to that of the longer-electrode specimen, introduced in Fig. 5(a), but the change ratio was negative. They demonstrated a decrease in the resistance when the crack passed through the virtual lines, and demonstrated a plateau in terms of negative values after the crack tip passed the virtual lines.

Similar to the previous specimen, the crack propagation length can be expressed in linear equations considering the relationship between the tensile extension, electrical resistance change of channel 2, and crack length as follows:

$$\text{Channel 1: } y_1 = 0.0013x_1 - 0.0177 \quad (7)$$

$$\text{Crack: } y_2 = 3.4528x_1 - 10.36 \quad (8)$$

$R^2$  of Eq. (7) was 0.9917, and that of Eq. (8) was 0.9380.

Similar previous studies showed the electromechanical behavior in the elastic regime [22,23] and casted a provision to delamination sensing [24]. Coupling mechanical deformation and change in electrical resistance now enables crack propagation monitoring with damage localization, specifically, in regard to crack propagation length.

### 3.3. Mode-I delamination test of HFRP

The mechanical properties deteriorated by replacing the length-wise carbon fiber wefts with glass fiber wefts, as shown in Fig. 6(d). The length-wise glass fiber tows, which replaced the carbon fiber tows, attributed to lowering the bending stiffness even though the width-wise warps were still carbon fibers. Comparing Figs. 5(c), (f), 6(c), and (g), the mechanical strength of HFRP was  $\sim 80$  N, whereas that of CFRP was  $\sim 110$  N. However, the maximum tensile extensions exceeded 2.2 times.

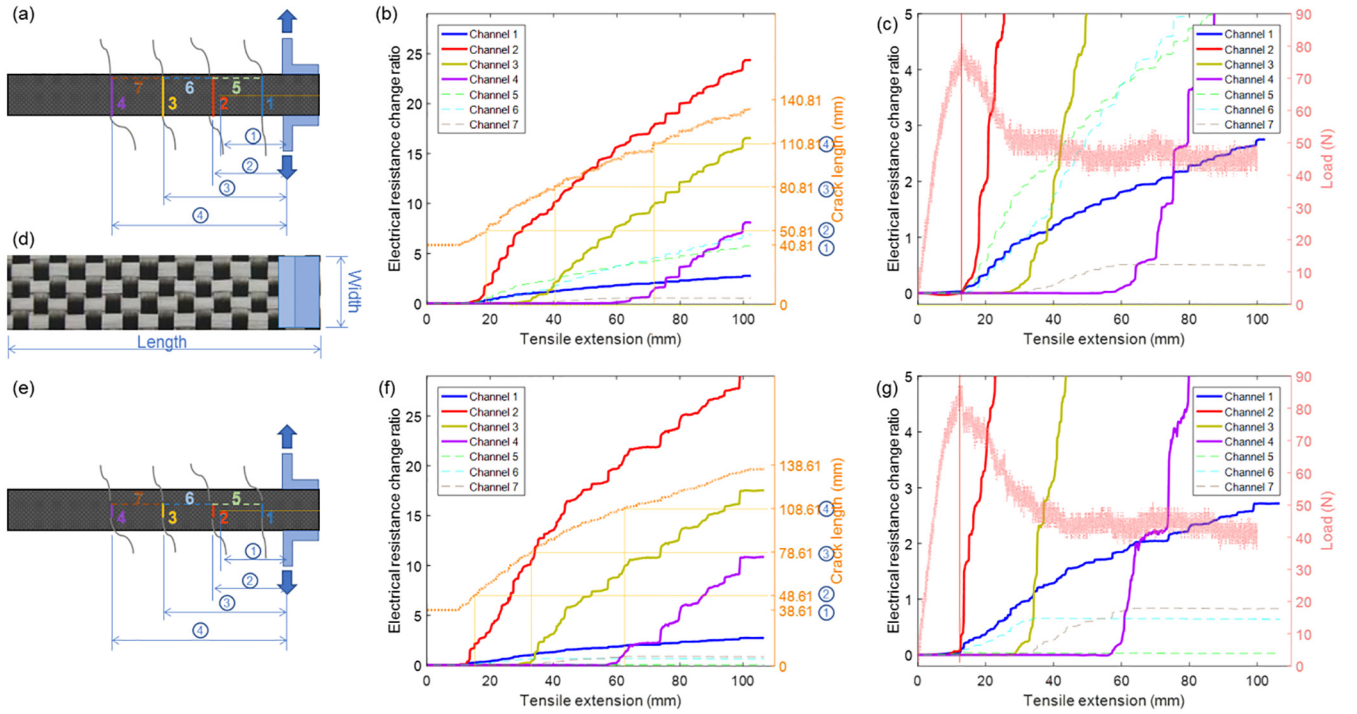


**Fig. 6.** (a) HFRP specimen with longer inter-electrode distance, (b) Electromechanical behavior of the longer inter-electrode distance HFRP compared to crack length, (c) Electromechanical behavior compared to load, (d) Top view of the hybrid fiber. (e) HFRP specimen with shorter inter-electrode distance, (f) Electromechanical behavior of the shorter inter-electrode HFRP compared to crack length, (g) Electromechanical behavior compared to load.

Insulative glass fiber tows, replaced with carbon fiber tows, reduced the electrical network; hence, the network breakage owing to crack propagation was more critical during the DCB tests than that of CFRPs. As a result, channel 1 of the HFRP specimens demonstrated 20 times more sensitivity than those of the CFRP specimens during crack propagation regardless of the type of electrode placement, as shown in Fig. 6(b) and (f). Considerably higher sensitivity was also observed in other channels. Moreover, channels 5–7 of HFRPs also demonstrated larger changes than those of CFRPs as compared in Figs. 5 and 6. The initial resistances of channels 1–4 were 65.8, 6.0, 6.6, and 5.3  $\Omega$ , respectively, and those of channels 5–7 were 3.2, 2.3, and 2.1  $\Omega$ , respectively, which were comparatively higher than those of CFRPs.

Due to the higher sensitivities of HFRPs, inter-tow and inter-ply interactions influence the change in electrical resistance. During bending, the in-plane, inter-tow distance was decreased at which in-plane compression was applied in the length-wise direction, leading to a decrease in electrical resistance. However, resistance increased outside the bending curvature where tension was applied, which was caused by tow separation, which counterbalances the compression-induced resistance decrease. Therefore, apparent electrical resistance changes were not observed in the elastic region.

Whereas the electrical resistance increased with higher sensitivity than that of CFRP when the crack propagated, the electromechanical behavior of HFRPs under the elastic region was not distinguishable. Fig. 6(c) and (g) are magnified images of the electrical resistance change ratio, to monitor the moment when the electrical resistance increased with structural failure. Thus, HFRPs are found to be more suitable for crack propagation detection due to higher sensitivity, rather than failure prognosis function under the elastic region.

In addition, electromechanical equations of channel 2 for the crack propagation length of the longer inter-electrode distance are as follows:

$$\text{Channel 1: } y_1 = 0.029x_1 - 0.0591 \quad (9)$$

$$\text{Crack: } y_2 = 1.1155x_1 - 11.43 \quad (10)$$

and those of the shorter inter-electrode distance are as follows:

$$\text{Channel 1: } y_1 = 0.0276x_1 - 0.0494 \quad (11)$$

$$\text{Crack: } y_2 = 1.1996x_1 - 12.29 \quad (12)$$

$R^2$  of Eq. (9) was 0.9766; Eq. (10), 0.9685; Eq. (11), 0.9601; and Eq. (12), 0.8719.

The electromechanical behavior of CFRP and HFRP is summarized in Fig. 7. CFRP was brittle compared with HFRP, and had a higher modulus and strength; therefore, the crack initiated in CFRP prior to HFRP. The HFRP had a fairly linear and higher sensitivity as the crack propagated, whereas the prognostic electrical response before crack initiation was observed in only CFRP.

### 3.4. Finite element analysis

The mechanical stress during the mode-I test was investigated and visualized using FEA. The mechanical stress of a CFRP in the through-thickness direction is shown in Fig. 8(a), and the stress along the mid-

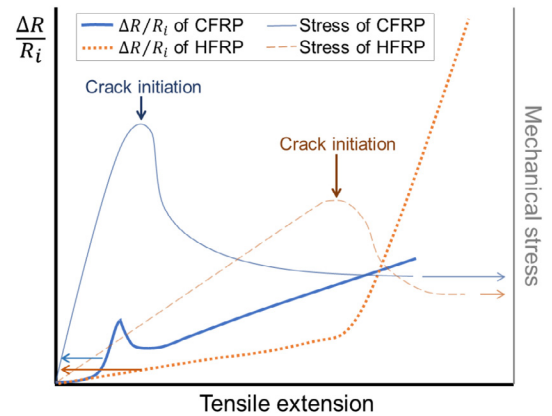


**Fig. 7.** Schematic of electromechanical behavior of CFRP and HFRP DCB specimen (blue and orange lines, respectively).

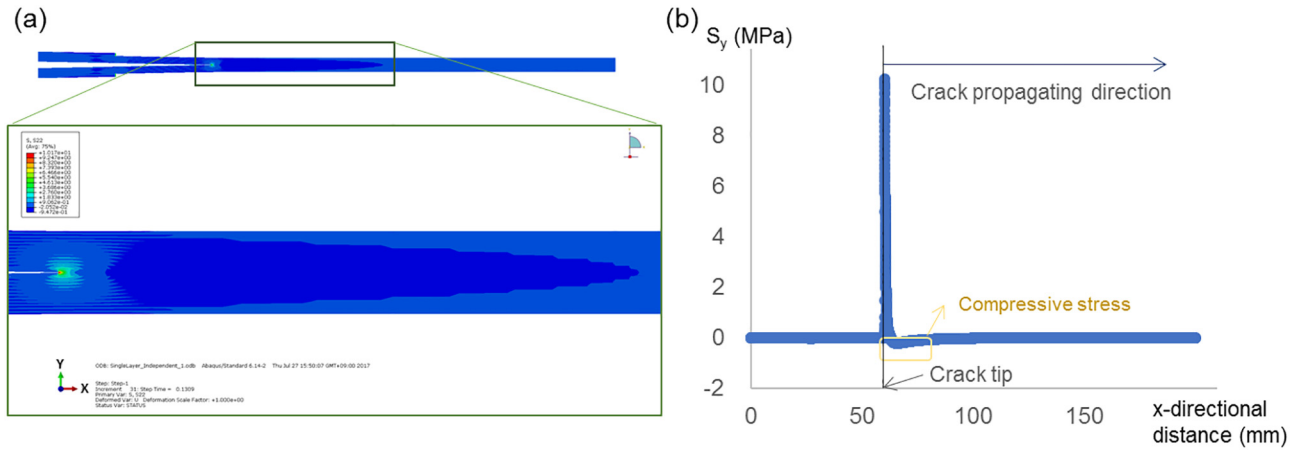


Fig. 8. (a) FEA of the CFRP DCB test, (b) Thickness-wise mechanical stress at the crack tip.

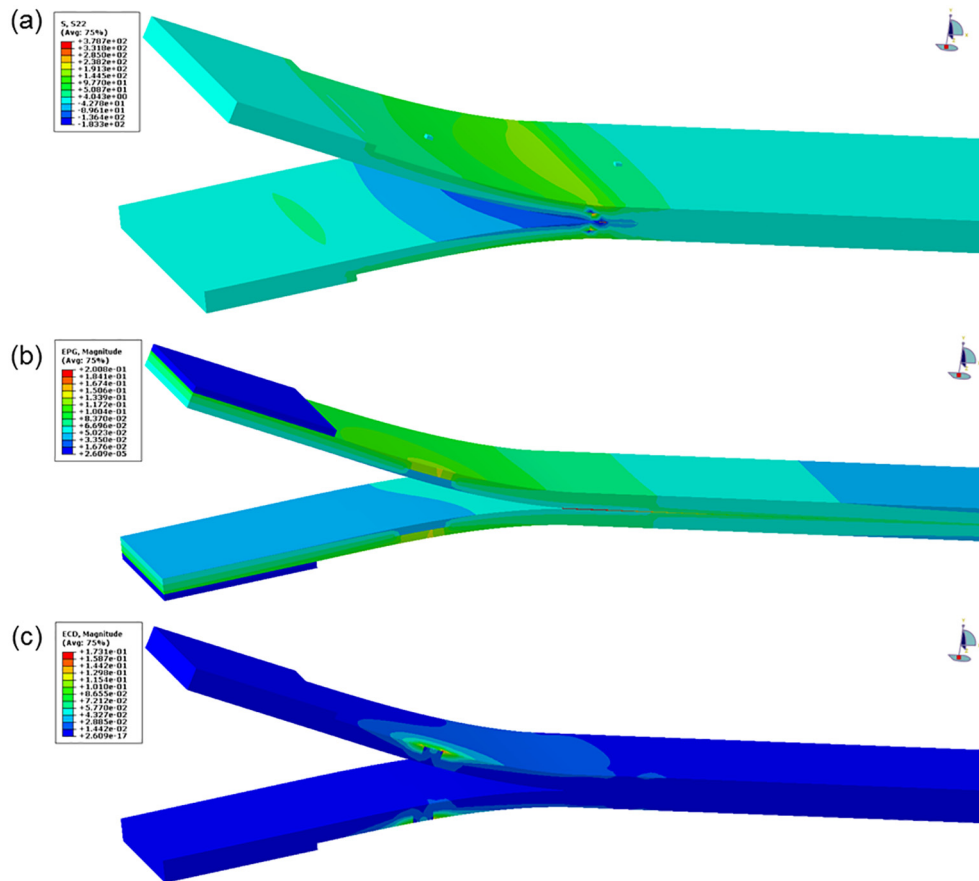


Fig. 9. (a) Mechanical stress of the CFRP, and cross-sectional view of (b) electrical potential gradient, and (c) electrical current density.

plane, which is the crack propagating path, is presented in Fig. 8(b). The graph in Fig. 8(b) represents the larger tensile stress at the crack tip and the compressive stress nearby. This simulation result rationalizes the changes in the electrical resistance of DCB specimens: A negative electrical resistance change was caused by the mechanical compressive stress when the crack approached the virtual electrode path nearby. On the other hand, change in the positive electrical resistance was caused by the mechanical tensile stress and electrical detour when the crack propagated through the virtual path.

FEA of a HFRP was also conducted, and similar results to Fig. 8 were attained, because the cohesive layer has identical properties. However, larger tensile displacement was required to initiate the same crack

length as that of CFRP, implying that further step was required to observe the same crack propagation. This is because the elastic modulus of the beam along the length was lower than that of CFRP; hence, a larger beam deflection of HFRP could be obtained with the same mechanical stress.

Electrical simulations verified that the electrical potential and current can cover the deformed area. This is presented in Fig. 9 with the cross-sectional views of the DCB specimens. The area of which the mechanical stress to be investigated as shown in Fig. 9(a) is similar to the coverage of the effective electrical current density as shown in Fig. 9(b) and electrical potential shown in Fig. 9(c). Thus, an effective electrical network can monitor the region for which the mechanical

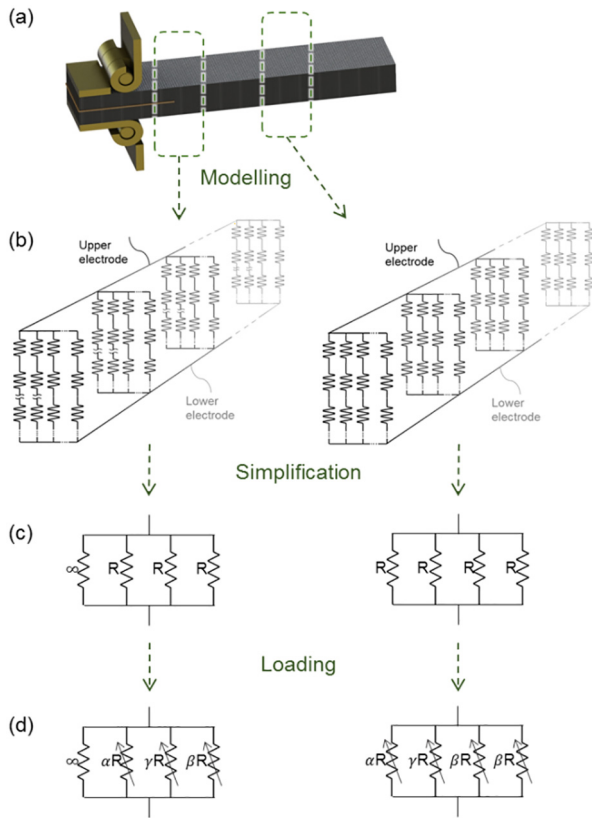


Fig. 10. Electrically equivalent circuit modelling process of a CFRP where  $\alpha > \beta > 1 > \gamma$  and crack propagates rightward. (a) Carbon-fiber-containing FRP. (b) Electrical network into electrical resistors. (c) Simplified equivalent circuit model. (d) Equivalent circuit model under mechanical loading.

deformation is required to be detected. Therefore, electrical FEA can aid in electrode placement design, which optimizes the location and the number of electrodes considering the mechanical deformation and the electrical current density.

### 3.5. Electrically equivalent circuit modelling

The electrical resistance change of CFRPs and HFRPs was modelled into an electrically equivalent circuit with resistors as shown in Fig. 10(a) and (b). This circuit contains the electrical network of intra-tow, inter-tow, and inter-ply.

The equivalent circuit model can be simplified into Fig. 10(c), which is an unloaded state, and 10(d), which is a loaded state.  $\alpha$ ,  $\beta$ , and  $\gamma$  are the tension, bending, and compression, respectively, which were determined from the FEA. The combination of these factors was the underlying rationale for the change in electrical resistance in terms of mode-I tensile extension, which was discussed in Section 3.3. The crack was regarded as an electrical network cut, so that its resistance value was represented as infinity in Fig. 10(c). The tension at the crack tip and the beam bending increased the resistance with multiplying factors of  $\alpha$  and  $\beta$ , respectively. However, the compression near the crack tip that was identified from Fig. 8(b) decreased the resistance; therefore,  $\gamma$ , which was less than 1, was multiplied. Based on the electrically equivalent circuit model and Eqs. (5)–(12), the overall electrical resistance change ratio enabled the SHM of the CFRPs and HFRPs. This model extended the electromechanical analysis of carbon fiber composites beyond the elastic regime, within which the electrically equivalent models were suggested in the previous studies [23,26].

## 4. Conclusions

The *in situ* self-sensing mechanism of CFRP was investigated based on the electromechanical behavior of conductive carbon fibers. The electrical network through the carbon fiber represented the electrical resistance change in terms of mechanical deformation. A mode-I delamination test indicated an increase in electrical resistance following the crack length, but decrease when the crack tip was near the virtual lines.

Carbon fiber-containing composites can be modified with different fiber stacking and electrode placements depending on the purpose: either prognostic function before crack initiation or crack length monitoring and damage localization with higher sensitivity.

The electromechanical response can be explained from the FEA results. The positive mechanical stress along the thickness and the negative stress adjacent to the crack tip are due to the electrical resistance changes during the mode-I tests. Based on the stress changes, the electrically equivalent model was proposed, and this enabled *in situ* SHM of CFRPs via electrical resistance changes. Therefore, the rationalized electromechanical behavior of carbon fibers containing composites can be employed for self-sensing prognostic and SHM systems.

## Acknowledgments

This work was supported by the National Research Foundation of Korea (NRF) grant funded by the Ministry of Science and ICT, Korea (NRF-2017R1A5A1015311) and the 2019 Research Fund (1.190011) of UNIST (Ulsan National Institute of Science and Technology).

## Data availability

The raw/processed data required to reproduce these findings cannot be shared at this time due to technical or time limitations.

## References

- [1] Sevillano E, Sun R, Gil A, Perera R. Interfacial crack-induced debonding identification in FRP-strengthened RC beams from PZT signatures using hierarchical clustering analysis. *Compos B Eng* 2016;87:322–35.
- [2] Kinet D, Mégret P, Goossen K, Qiu L, Heider D, Caucheteur C. Fiber Bragg grating sensors toward structural health monitoring in composite materials: challenges and solutions. *Sensors* 2014;14(4):7394–419.
- [3] Kianmofrad F, Ghafouri E, Elyasi MM, Motavalli M, Rahimian M. Strengthening of metallic beams with different types of pre-stressed un-bonded retrofit systems. *Compos Struct* 2017;159:81–95.
- [4] You Y-J, Kim J-H, Kim S-J, Park Y-H. Methods to enhance the guaranteed tensile strength of GFRP rebar to 900MPa with general fiber volume fraction. *Constr Build Mater* 2015;75:54–62.
- [5] Ruzek R, Kudrna P, Kadlec M, Karachalios V, Tserpes KI. Strain and damage monitoring in CFRP fuselage panels using fiber Bragg grating sensors. Part II: mechanical testing and validation. *Compos Struct* 2014;107:737–44.
- [6] Liu Y, Hu N, Xu H, Yuan W, Yan C, Li Y, et al. Damage evaluation based on a wave energy flow map using multiple PZT sensors. *Sens* 2014;14(2):1902–17.
- [7] Gao D, Wang Y, Wu Z, Rahim G, Bai S. Design of a sensor network for structural health monitoring of a full-scale composite horizontal tail. *Smart Mater Struct* 2014;23:1–11.
- [8] Giridhara G, Rathod VT, Naik S, Roy Mahapatra D, Gopalakrishnan S. Rapid localization of damage using a circular sensor array and Lamb wave based triangulation. *Mech Syst Signal Process* 2010;24(8):2929–46.
- [9] Qiu L, Liu B, Yuan S, Su Z, Ren Y. A scanning spatial-wavenumber filter and PZT 2-D cruciform array based on-line damage imaging method of composite structure. *Sens Actuata A* 2016;248:62–72.
- [10] Li F, Peng H, Meng G. Quantitative damage image construction in plate structures using a circular PZT array and lamb waves. *Sens Actuata A* 2014;214:66–73.
- [11] Shrestha P, Kim J-H, Park Y, Kim C-G. Impact localization on composite wing using 1D array FBG sensor and RMS/correlation based reference database algorithm. *Compos Struct* 2015;125:159–69.
- [12] Stutz S, Cugnoni J, Botsis J. Studies of mode I delamination in monotonic and fatigue loading using FBG wavelength multiplexing and numerical analysis. *Compos Sci Technol* 2011;71(4):443–9.
- [13] Canal LP, Sarfaraz R, Violakis G, Botsis J, Michaud V, Limberger HG. Monitoring strain gradients in adhesive composite joints by embedded fiber Bragg grating sensors. *Compos Struct* 2014;112:241–7.
- [14] Kesavan K, Ravisankar K, Senthil R, Farvaze Ahmed AK. Experimental studies on performance of reinforced concrete beam strengthened with CFRP under cyclic loading using FBG array. *Meas* 2013;46(10):3855–62.



- [15] Di Sante R. Fibre optic sensors for structural health monitoring of aircraft composite structures: recent advances and applications. *Sens* 2015;15(8):1–48.
- [16] Leng J, Asundi A. SHM of smart composite materials by using EPFI and FBG sensors. *Sens Actuat A* 2003;103:330–40.
- [17] Guo H, Xiao G, Mrad N, Yao J. Fiber optic sensors for structural health monitoring of air platforms. *Sens* 2011;11(4):3687–704.
- [18] Lee J-R, Ciang Chia C, Park C-Y, Jeong H. Laser ultrasonic anomalous wave propagation imaging method with adjacent wave subtraction: algorithm. *Opt Laser Technol* 2012;44(5):1507–15.
- [19] Yu L, Tian Z. Lamb wave structural health monitoring using a hybrid PZT-laser vibrometer approach. *Struct Health Monit* 2013;12(5–6):469–83.
- [20] Wang X, Chung DDL. Short carbon fiber epoxy-matrix composite as a piezoresistive strain sensor. *Smart Mater Struct* 1995;4:363–7.
- [21] Wang D, Chung DDL. Through-thickness piezoresistivity in a carbon fiber polymer-matrix structural composite for electrical-resistance-based through-thickness strain sensing. *Carbon* 2013;60:129–38.
- [22] Wen J, Xia Z, Choy F. Damage detection of carbon fiber reinforced polymer composites via electrical resistance measurement. *Compos B* 2011;42(1):77–86.
- [23] Park JB, Okabe T, Takeda N, Curtin WA. Electromechanical modeling of unidirectional CFRP composites under tensile loading condition. *Compos A* 2002;33(2):267–75.
- [24] Todoroki A, Samejima Y, Hirano Y, Matsuzaki R. Piezoresistivity of unidirectional carbon/epoxy composites for multiaxial loading. *Compos Sci Technol* 2009;69(11–12):1841–6.
- [25] Todoroki A, Omagari K, Shimamura Y, Kobayashi H. Matrix crack detection of CFRP using electrical resistance change with integrated surface probes. *Compos Sci Technol* 2006;66(11–12):1539–45.
- [26] Todoroki A, Tanaka M, Shimamura Y. Measurement of orthotropic electric conductance of CFRP laminates and analysis of the effect on delamination monitoring with an electric resistance change method. *Compos Sci Technol* 2002;62(5):619–28.
- [27] Swait TJ, Jones FR, Hayes SA. A practical structural health monitoring system for carbon fibre reinforced composite based on electrical resistance. *Compos Sci Technol* 2012;72(13):1515–23.
- [28] Schueler R, Joshi SP, Schulte K. Damage detection in CFRP by electrical conductivity mapping. *Compos Sci Technol* 2001;61(6):921–30.
- [29] Kupke M, Schulte K, Schüler R. Non-destructive testing of FRP by d.c. and a.c. electrical methods. *Compos Sci Technol* 2001;61(6):837–47.
- [30] Xiao J, Li Y, Fan WX. A laminate theory of piezoresistance for composite laminates. *Compos Sci Technol* 1999;59(9):1369–73.
- [31] Ogi K, Takao Y. Characterization of piezoresistance behavior in a CFRP unidirectional laminate. *Compos Sci Technol* 2005;65(2):231–9.
- [32] Park JK, Cho D, Kang TJ. A comparison of the interfacial, thermal, and ablative properties between spun and filament yarn type carbon fabric/phenolic composites. *Carbon* 2004;42(4):795–804.
- [33] ASTM D790 Standard Test Methods for Flexural Properties of Unreinforced and Reinforced Plastics and Electrical Insulating Materials. *ASTM Int.*; 2018.
- [34] Shen L, Li J, Liaw BM, Delale F, Chung JH. Modeling and analysis of the electrical resistance measurement of carbon fiber polymer-matrix composites. *Compos Sci Technol* 2007;67(11–12):2513–20.
- [35] Neyestanek AAL, Nazari SA, Sadeghbeigi N, Karimzadeh A. Electrical behaviour of glass/carbon- phenolic conductive hybrid composite woven used in electrostatics precipitator filter. *Int J Electrochem Sci* 2014;9:6416–30.